

Article

## Synthesis and Exfoliation of a New Layered Mesoporous Zr-MOF Comprising Hexa- and Dodecanuclear Clusters as well as a Small Organic Linker Molecule

Sebastian Leubner, Viktor E.G. Bengtsson, Kevin Synnatschke, Jonas Gosch, Alexander Koch, Helge Reinsch, Hongyi Xu, Claudia Backes, Xiaodong Zou, and Norbert Stock

*J. Am. Chem. Soc.*, **Just Accepted Manuscript** • DOI: 10.1021/jacs.0c06978 • Publication Date (Web): 21 Aug 2020

Downloaded from [pubs.acs.org](https://pubs.acs.org) on August 21, 2020

### Just Accepted

“Just Accepted” manuscripts have been peer-reviewed and accepted for publication. They are posted online prior to technical editing, formatting for publication and author proofing. The American Chemical Society provides “Just Accepted” as a service to the research community to expedite the dissemination of scientific material as soon as possible after acceptance. “Just Accepted” manuscripts appear in full in PDF format accompanied by an HTML abstract. “Just Accepted” manuscripts have been fully peer reviewed, but should not be considered the official version of record. They are citable by the Digital Object Identifier (DOI®). “Just Accepted” is an optional service offered to authors. Therefore, the “Just Accepted” Web site may not include all articles that will be published in the journal. After a manuscript is technically edited and formatted, it will be removed from the “Just Accepted” Web site and published as an ASAP article. Note that technical editing may introduce minor changes to the manuscript text and/or graphics which could affect content, and all legal disclaimers and ethical guidelines that apply to the journal pertain. ACS cannot be held responsible for errors or consequences arising from the use of information contained in these “Just Accepted” manuscripts.

# Synthesis and Exfoliation of a New Layered Mesoporous Zr-MOF Comprising Hexa- and Dodecanuclear Clusters as well as a Small Organic Linker Molecule

Sebastian Leubner,<sup>a</sup> Viktor E.G. Bengtsson,<sup>b</sup> Kevin Synnatschke,<sup>c</sup> Jonas Gosch,<sup>a</sup> Alexander Koch,<sup>a</sup> Helge Reinsch,<sup>a</sup> Hongyi Xu,<sup>b</sup> Claudia Backes,<sup>c\*</sup> Xiaodong Zou<sup>b\*</sup> and Norbert Stock<sup>a\*</sup>

<sup>a</sup> Institute of Inorganic Chemistry, University of Kiel, Max-Eyth Strasse 2, 24118 Kiel (Germany).

<sup>b</sup> Department of Materials and Environmental Chemistry, Stockholm University, SE-106 91 Stockholm (Sweden).

<sup>c</sup> Institute of Physical Chemistry, Heidelberg University, Im Neuenheimer Feld 253, 69120 Heidelberg (Germany).

**ABSTRACT:** A new layered mesoporous Zr-MOF of composition  $[\text{Zr}_{30}\text{O}_{20}(\text{OH})_{26}(\text{OAc})_{18}\text{L}_{18}]$  was synthesized employing 5-acetamidisophthalic acid ( $\text{H}_2\text{L}$ ) in acetic acid as the solvent. The new MOF, denoted as CAU-45, exhibits a honeycomb structure of stacked layers which comprise both hexa- and dodecanuclear zirconium clusters. Its structure was solved from submicron-sized crystals by continuous rotation electron diffraction (cRED). Liquid phase exfoliation and size selection were successfully performed on the material.

## Introduction

Metal-organic frameworks (MOFs) are potentially porous coordination networks. They are assembled from inorganic nodes, also called inorganic building units (IBUs), which are interconnected by organic linker molecules.<sup>[1,2]</sup> MOFs are promising candidates for multiple applications such as gas storage<sup>[3]</sup> and separation,<sup>[4]</sup> catalysis,<sup>[5,6]</sup> water harvesting,<sup>[7]</sup> heat transformation,<sup>[8,9]</sup> drug carriers,<sup>[10,11]</sup> sensors<sup>[12–14]</sup> or imaging materials.<sup>[15]</sup> For some of these applications, like catalysis or drug delivery, mesoporous MOFs are especially valuable due to their large pores.<sup>[16,17]</sup>

Zirconium based MOFs (Zr-MOFs) usually exhibit high thermal and chemical stability<sup>[18]</sup> and even mesoporous materials can be obtained by employing very large organic linker molecules. The size of these linkers intrinsically enables the formation of large pores, but they also tend to increase susceptibility towards framework collapse.<sup>[17]</sup> In general, the stability of Zr-MOFs arises from strong zirconium-oxygen bonds between the  $\text{Zr}^{4+}$  centers and the ligands as well as from the high connectivity of the IBUs.<sup>[18,19]</sup>

The most frequently observed IBU in Zr-MOFs is the hexanuclear  $[\text{Zr}_6(\mu_3\text{-O})_4(\mu_3\text{-OH})_4]^{12+}$  cluster.<sup>[19,20]</sup> Recently, dodecanuclear  $[\text{Zr}_{12}(\mu_3\text{-O})_8(\mu_3\text{-OH})_8(\mu\text{-OH})_6]^{18+}$  clusters were discovered, comprising two hexanuclear clusters which are condensed via three shared edges.<sup>[21–24]</sup> If these are only connected via one shared edge, an infinite one dimensional (1D) IBU  $(\infty\{[\text{Zr}_6(\mu_3\text{-O})_4(\mu_3\text{-OH})_4(\mu\text{-OH})_2]\})$  can be obtained, as observed in CAU-22.<sup>[25]</sup> Moreover, whole  $\{\text{ZrO}_8\}$  polyhedra can be shared, leading to a 1D IBU  $(\infty\{[\text{Zr}_5(\mu_3\text{-O})_4(\mu_3\text{-OH})_4]\})$  with an even higher degree of condensation, as demonstrated with CAU-27 in one of our latest studies.<sup>[26]</sup> In that approach, we described the solvothermal synthesis of new dicarboxylate zirconium MOFs via the utilization of acetic acid as a green alternative solvent.<sup>[27,28]</sup> Acetic acid is available in such high excess, that acetate ligands are incorporated into the structure

of the product. They occupy coordination sites on the IBUs which would be otherwise saturated by linker molecules, leading to uncommon network topologies for Zr-MOFs.<sup>[26]</sup>

Layered MOFs can be exfoliated to sheet stacks via top-down approaches. The individual layers are held together by weak interactions like van der Waals forces, hydrogen bonds or dielectric interactions and can potentially be separated into 2D nanosheets if these interactions are weaker than the in-plane bonding.<sup>[29]</sup> An increasingly popular approach to produce colloidally stable 2D nanosheet inks is liquid phase exfoliation (LPE).<sup>[30,31]</sup> This process has been applied to various inorganic van der Waals crystals<sup>[32,33]</sup> and very recently also to organic 2D structures.<sup>[34]</sup> The nanosheets from this approach are polydisperse in size and thickness. This enables the selection of defined sizes by centrifugation-based techniques,<sup>[35]</sup> for example liquid cascade centrifugation (LCC),<sup>[36]</sup> and thus the isolation of nanomaterials tailored to the needs of specific applications. Especially, uses in catalysis, sensors or nanomedicine can profit from nano-sized MOF particles, due to their high internal and external surface areas as well as controllable functionality.<sup>[29]</sup>

In this work, we expanded our acetic acid based synthetic approach further to a small functionalized linker molecule with bent geometry ( $\text{H}_2\text{L}$ :  $\text{C}_8\text{H}_5\text{O}_4\text{-NHOAc}$ , Fig. 1) and present the new layered mesoporous Zr-MOF  $[\text{Zr}_{30}\text{O}_{20}(\text{OH})_{26}(\text{OAc})_{18}\text{L}_{18}]$ , denoted as CAU-45, together with a suitable liquid phase exfoliation and size selection route.

## Results and Discussion

CAU-45 with low crystallinity was first discovered in a high throughput<sup>[37]</sup> linker screening upon reacting 5-aminoisophthalic acid with zirconium acetate in glacial acetic acid at 160 °C under solvothermal conditions (see SI section 1.3, Tab. S1.3.1). 5-aminoisophthalic acid was transformed to 5-acetamidisophthalic acid during this procedure, which

represents a limiting step, since the actual linker molecule required for the formation of CAU-45 turned out to be the latter. Therefore, an optimized route was developed. It comprises the direct use 5-acetamidoisophthalic acid under otherwise similar conditions (Fig. 1). Synthetic details are given in the supporting information.

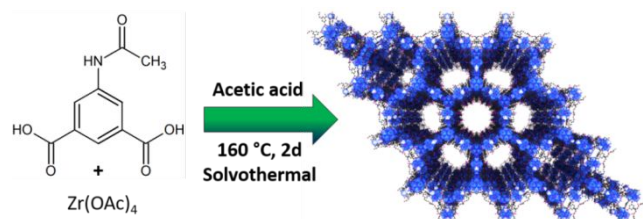


**Figure 1.** Optimized synthesis procedure for CAU-45.

The bulk powder sample of CAU-45 consists mostly of tapered rod-shaped crystals with lateral sizes of ca. 0.3 - 3  $\mu\text{m}$  and diameters of up to  $\sim 0.7 \mu\text{m}$  (Fig. 2A). Continuous rotation electron diffraction (cRED) was used to determine the structure of CAU-45, which shows CAU-45 crystallizes in the hexagonal space group  $P6_3/mmc$  with  $a = 33.802(4)$  and  $c = 29.096(5)$   $\text{\AA}$  and the  $c$ -axis is aligned along the rod direction. In order to reduce the electron beam damage, a fast hybrid Timepix electron detector in combination with a fast crystal rotation speed ( $1.13^\circ\text{s}^{-1}$ ) was used. The data collection time for a cRED dataset was less than 1.5 min and the data resolution is better than 0.8  $\text{\AA}$ . Figure 2B presents a typical crystal selected for cRED measurements. Figures 2C and D show the reciprocal lattice reconstructed from typical cRED data. In order to increase the data completeness and quality, cRED data sets from multiple crystals were combined.<sup>[38]</sup> Hierarchical cluster analysis was performed on data sets from 29 crystals. 18 of them show the best agreement in terms of both the unit cell parameters and reflection intensities, and were therefore merged for the final structure determination.<sup>[39]</sup> The structure was solved by direct methods and all non-H atoms could be located directly either from the structure solution or from the difference Fourier maps in the subsequent structure refinement. Details on the cRED data collection, data analysis and structure determination are given in the Supporting Information in section S2.2, Table S2.2.1 and Figures. S2.2.1-2.2.3. The powder X-ray diffraction (PXRD) pattern simulated from the structural model of CAU-45 obtained by cRED reveals a good match to the measured PXRD pattern (Fig. S2.1.3), and thus confirms a successful structure determination. To the best of our knowledge, CAU-45 is the first example of a mesoporous MOF solved by direct phasing of electron diffraction data without the need of model building.<sup>[40,41]</sup> The high resolution and high quality data also make it possible to perform the structure refinement ( $R1 = 0.2253$  for 8769 reflections and 335 parameters) so that the hydrogen bond network and disorders of the amide groups can be identified.

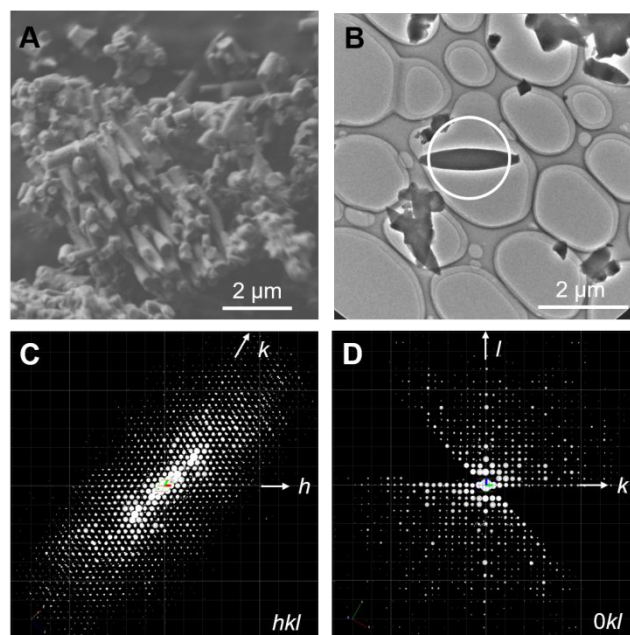


**Figure 2.** Scanning electron microscopy (SEM) micrograph of a powder sample (A), transmission electron microscopy (TEM) micrograph of a typical crystal used for cRED measurements (B), reconstructed 3D reciprocal lattice of a typical dataset reconstructed with REDp<sup>[42]</sup> viewed along the  $c^*$ -axis (C) and a  $0kl$  slice from the same reconstruction (D).

The following structure description assumes the presence of H-atoms and H-bonds. H-atoms in the IBUs are assigned according to literature data,<sup>[19]</sup> while the discussion of H-bonding is based on donor-acceptor distances. CAU-45 contains two different IBUs, the well-known hexanuclear  $[Zr_6(\mu_3-O)_4(\mu_3-OH)_4]^{12+}$  cluster (Fig. 3, A) and the less frequently observed dodecanuclear  $[Zr_{12}(\mu_3-O)_8(\mu_3-OH)_8(\mu-OH)_6]^{18+}$  cluster (Fig. 3, B). To the best of our knowledge, this is the first example of hexa- and dodecanuclear clusters occurring simultaneously in a Zr-MOF structure. So far, only mixed hexanuclear and octanuclear clusters  $[Zr_8O_6(OH)_8]^{12+}$  could be observed in NPF-200 and -201 by Zhang *et al.* in 2016.<sup>[43]</sup> Within the CAU-45 structure, both cluster types are partly capped by acetate ligands. The hexanuclear clusters exhibit four acetate ligands per cluster ( $[Zr_6(\mu_3-O)_4(\mu_3-OH)_4(OAc)_4]^{8+}$ ) and the dodecanuclear clusters exhibit six acetate ligands per cluster ( $[Zr_{12}(\mu_3-O)_8(\mu_3-OH)_8(\mu-OH)_6(OAc)_6]^{12+}$ ) (Fig. 3, A, B). Therefore, the potential coordination sites for linker carboxylate groups are reduced from 12 to 8 and from 18 to 12, respectively. Consequently, each hexanuclear  $[Zr_6(\mu_3-O)_4(\mu_3-OH)_4]^{12+}$  cluster connects to eight linkers and each dodecanuclear  $[Zr_{12}(\mu_3-O)_8(\mu_3-OH)_8(\mu-OH)_6]^{18+}$  cluster connects to twelve linkers.

Three hexanuclear  $[Zr_6(\mu_3-O)_4(\mu_3-OH)_4]^{12+}$  clusters form a trimer, connected by three pairs of the 5-acetamidoisophthalate linkers via their carboxylate groups. There are two trimers and two dodecanuclear  $[Zr_{12}(\mu_3-O)_8(\mu_3-OH)_8(\mu-OH)_6]^{18+}$  clusters in each unit cell. All are located on the 3-fold axis, i.e.  $(1/3, 2/3, \pm 1/4)$  or  $(2/3, 1/3, \pm 1/4)$ . Each dodecanuclear cluster connects to three trimers and each trimer connects to three dodecanuclear clusters by six pairs of the linkers via their carboxylate groups to form a layer with an overall composition of  $(\{ [Zr_6(\mu_3-O)_4(\mu_3-OH)_4(OAc)_4]_3 \{ Zr_{12}(\mu_3-O)_8(\mu_3-OH)_8(\mu-OH)_6(OAc)_6 \} (C_8H_3O_4-NHAc)_{18} \})$  (Fig. 3). There are two layers in each unit cell,

related by a  $6_3$  symmetry, which stack with alternating trimer and dodecanuclear cluster along the  $c$ -axis.

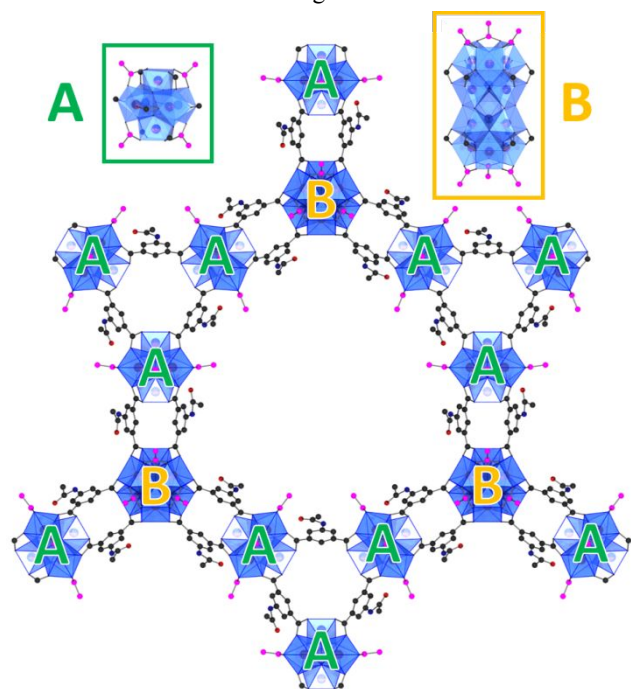


**Figure 3.** Inorganic building units (IBUs) of CAU-45 and interconnection to a layer motive via 5-acetamidoisophthalate ions. **A:** Hexanuclear clusters. **B:** Dodecanuclear clusters. Linker carbon atoms are displayed in black and acetate carbon atoms in pink. Zirconium: bronze, oxygen: red, nitrogen: dark blue, hydrogen: not displayed. Zirconium-oxygen clusters: blue.

The layers are held together by a network of hydrogen bonds, being formed between neighboring linker amide groups (Fig. 4, left). Since neighboring amide groups within the structure of CAU-45 never originate from the same layer, a relatively strong layer-layer interaction is established. It is likely that the hydrogen bonding is crucial for the formation of CAU-45, since the MOF could not be obtained with other related linker molecules, like isophthalic acid for example (Tab. S1.3.1). The overall CAU-45 network forms large hexagonal-shaped channels (Fig. 4, right). Per pore, each layer is connected to the next layer by 18 hydrogen bonds. Six acetate ligands per formula unit, which exclusively originate from hexanuclear clusters, point directly into the pore channels, opening up possibilities for postsynthetic modifications. Examples would be ligand exchange or removal, which have been already realized for various Zr-MOFs.<sup>[26,44–48]</sup> The widest section of the channels can accommodate a non-colliding sphere with a diameter of  $\sim 22$  Å (Fig. S2.2.9), while the narrowest (limited by the steric demand of the acetate ligands) has a diameter of  $\sim 17$  Å. A more in-depth structure description is given in the SI.

The composition of CAU-45 was confirmed with various characterization techniques such as thermogravimetric (TGA) and elemental analysis (EA) as well as  $^1\text{H}$  nuclear magnetic resonance (NMR), Infrared (IR) and Raman spectroscopy (details are given in the SI).

Nitrogen and water adsorption/desorption experiments were carried out in order to investigate sorption properties of the material. According to the IUPAC (International Union of Pure and Applied Chemistry) guidelines for the physisorption of gases,<sup>[49]</sup> CAU-45 exhibits a type IV(b) nitrogen adsorption

isotherm which is characteristic for mesoporous adsorbents (Fig. S2.5.1). The maximum water adsorption capacity is 330 mg/g (Fig. S2.5.2). Variable-temperature (VT) PXRD and TGA measurements indicate a thermal stability up to 330 °C in air (SI section 2.4). 24 h solvent stability tests with common organic liquids and aqueous solutions of different pH (1–13) were carried out with CAU-45 (Tab. S2.10.1). The material remained crystalline in 16 out of 23 tests.

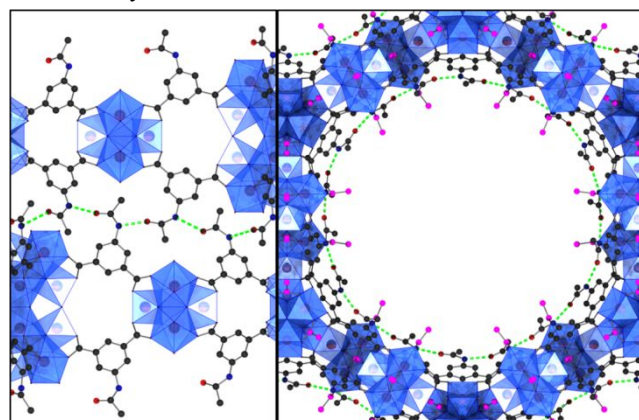


**Figure 4.** Two stacked layers of CAU-45 viewed along [110] (left) and [001] (right). The layers are held together by hydrogen bonds between the N-H protons and C=O oxygen atoms of neighboring linker amide groups. Since proton positions could not be located, hydrogen bonds are represented as dashed green lines between amide nitrogen and oxygen atoms. Linker carbon atoms are displayed in black and acetate carbon atoms in pink. Zirconium: bronze, oxygen: red, nitrogen: dark blue, hydrogen: not displayed. Zirconium-oxygen clusters: blue.

The layered structure should enable exfoliation. To demonstrate this, inks of delaminated CAU-45 containing different sizes of nanosheets were prepared using LPE in aqueous surfactant solution coupled with centrifugation-based size selection according to established protocols as detailed in the SI. As a first approach, the structural integrity upon exfoliation was tested. A stock dispersion was prepared by ultrasonication and incompletely exfoliated material was removed at low centrifugal acceleration (400 g, expressed in multiples of the earth's gravitational force, g). The dispersion was subsequently concentrated by sedimenting the nanosheets at 74k g and characterized via PXRD (dried dispersion) as well as Raman measurements (drop-cast dispersion). Since the comparison of bulk and exfoliated material (Fig. S2.9.1) does not show any differences with respect to the characteristic features, the structure of the MOF can be considered intact after the exfoliation. The nanosheet yield after removal of the mostly unexfoliated material after centrifugation at 50 g was determined to be 38.0% by gravimetric filtering. However, due to the strong interlayer interactions, the nanomaterial isolated is thicker than observed for other 2D-materials of the same lateral dimensions. If the material sedimented at speeds up to 400 g (i.e.  $\langle T \rangle \leq 80$  nm) is considered as nanosheets, the yield of the exfoliation would decrease to 4.3%. We would like to point out, that the yield of the exfoliation mostly depends on what is considered as nanomaterial.

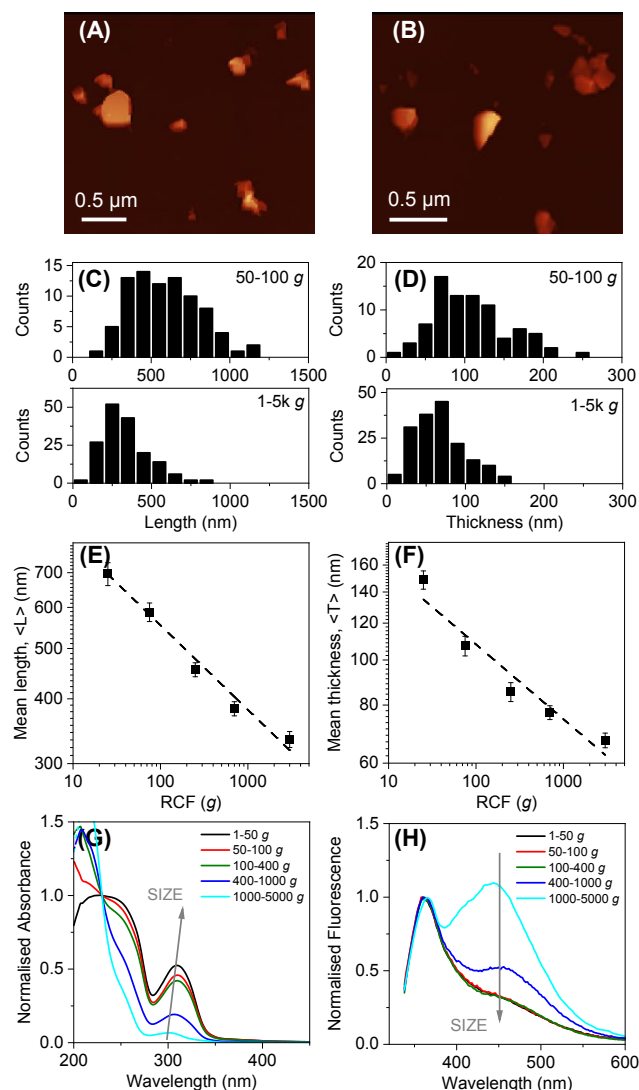


**Figure 5.** Liquid phase exfoliation. AFM images of relatively large (50-100 g, A) and small (1-5k g, B) drop-cast nanosheets after LPE and LCC. The images show representative nanosheets of the respective fractions. (C-D) Histograms of lateral sheet size (C) and thickness (D) distribution of two above mentioned fractions of size-selected nanosheets. (E+F) Plot of arithmetic mean nanosheet length,  $\langle L \rangle$  (E) and thickness,  $\langle T \rangle$  (F) as a function of the midpoint of centrifugal accelerations used during size selection. The data in (E) and (F) is characterized by a power law scaling as indicated by the dashed line. (G-H) Normalized absorbance (G) and fluorescence (H) spectra measured with an excitation wavelength of 325 nm of different sizes of nanosheets. Size dependent changes in (G-H) are highlighted by a grey arrow.

To achieve size selection, LCC was performed on the stock dispersion involving consecutive centrifugation steps with iteratively increasing centrifugation speeds. After each centrifugation step, the sediment was redispersed at increased nanosheet concentration and analyzed, while the supernatant was subjected to centrifugation at higher speeds. In this way, five fractions were isolated and labelled by the boundaries of centrifugal accelerations between two steps (Fig. S2.9.2). The nanosheet dimensions were determined by statistical atomic force microscopy (AFM) measurements (Fig. 5 A-D, Fig. S2.9.4 and S2.9.5). From images such as in Figure 5 A-B, the longest dimensions (length,  $L$ ), and thickness ( $T$ ) of each nanosheet were measured to obtain distribution histograms

(Fig. 5 C-D, Fig. S2.9.4). Mean size and thickness of the nanosheets follow the typical power law dependence with respect to the midpoint of the centrifugation speed (central RCF) between two steps (Fig. 5 E-F).<sup>[32,36,50]</sup>

The mean lateral size can be varied between 300 and 700 nm, with thicknesses ranging from 60-150 nm and a length/thickness aspect ratio centered around 6 which is similar to layered hydroxides.<sup>[32]</sup>

This clearly demonstrates both successful exfoliation, as well as size selection. Systematic size dependent changes are observed in absorbance (Fig. 5G and Fig. S2.9.6), extinction (Fig. S2.9.6) and fluorescence measurements (Fig. 5 H and Fig. S2.9.7). This behavior is typical for 2D nanomaterial dispersions<sup>[34,36,51-53]</sup> and commonly attributed to a combination of light scattering<sup>[53]</sup> (in extinction spectra), edge<sup>[34,51]</sup> as well as dielectric screening and confinement effects.<sup>[51,52]</sup> Each effect changes spectra in a characteristic way. In the case of CAU-45, we attribute the spectral changes shown mostly due to edge effects. It allows to develop spectroscopic metrics for the mean size of the nanosheets in the ink which is useful for future work to assess the size dependent application potential. For a detailed discussion see SI.

## Conclusion

The discovery and characterization of the thermally (up to 330 °C in air) and chemically stable layered mesoporous zirconium MOF CAU-45  $[\text{Zr}_{30}\text{O}_{20}(\text{OH})_{26}(\text{OAc})_{18}\text{L}_{18}]$  is reported. The compound was synthesized by reacting zirconium acetate with the small bent-geometry linker molecule 5-acetamidophthalic acid ( $\text{H}_2\text{L}$ ) under solvothermal conditions in acetic acid, a green solvent. Continuous rotation electron diffraction (cRED) was used for the structure determination of CAU-45. Its structure features hexa- and dodecanuclear zirconium-oxygen clusters as IBUs and large hexagonal pores with a diameter of ca. 17 Å in its narrowest and 22 Å in its widest sections. Per formula unit, a total of 18 acetate ligands are capping otherwise free coordination sites on the IBUs, whereof six are directly pointing towards the center of the pore, opening up possibilities for postsynthetic modifications. The layers of the material are held together by a large number of hydrogen bonds, which adds up to 18 per pore channel at the layer intersection. These bonds are established between neighboring linker amide groups via their N-H protons and C=O oxygen atoms to form a circular connection scheme along the pore wall, perpendicular to the crystallographic  $c$ -axis. In spite of this relatively strong out of plane bonding, we demonstrate that exfoliation by LPE is possible which allows to produce inks of structurally intact CAU-45 nanosheets that can be size-selected by centrifugation. The inherent solution processability in combination with the tuneability of size are the prerequisite to test CAU-45 in various application areas for example catalysis, gas and ion separation or sensing in future work.

## ASSOCIATED CONTENT

### Supporting Information

The Supporting Information is available free of charge on the ACS Publications website. It contains the utilized chemicals and instruments, synthetic procedures, detailed structural analysis by cRED and structure description, powder X-ray diffraction (PXRD) and variable temperature (VT) PXRD data, thermogravimetric (TGA) and elemental analyses (EA), infrared (IR) and RAMAN

spectra, scanning electron microscopy (SEM) and atomic force microscopy (AFM) micrographs, nitrogen and water sorption isotherms, <sup>1</sup>H nuclear magnetic resonance (NMR) analysis as well as UV-Vis and fluorescence measurements (PDF file). The CAU-45 crystal structure is deposited as CIF file and also available from the Cambridge Crystallographic Data Centre (CCDC) under entry number 2012374.

## AUTHOR INFORMATION

### Corresponding Authors

Prof. Dr. N. Stock, Institute of Inorganic Chemistry, University of Kiel, Max-Eyth Strasse 2, 24118 Kiel (Germany). E-mail: stock@ac-uni-kiel.de

Prof. Dr. X. Zou, Department of Materials and Environmental Chemistry, Stockholm University, SE-106 91 Stockholm (Sweden). E-mail: xzou@mmk.su.se

Dr. C. Backes, Institute of Physical Chemistry, Heidelberg University, Im Neuenheimer Feld 253, 69120 Heidelberg (Germany). E-mail: backes@uni-heidelberg.de

### Notes

The authors declare no competing financial interests.

## ACKNOWLEDGMENT

X.Z. acknowledges support from the Swedish Research Council (VR, 2017-04321) and the Knut and Alice Wallenberg Foundation (KAW, 2012-0112). C.B. acknowledges support from the German Research Foundation (DFG) under grant agreement Emmy-Noether, BA4856/2-1, and Jana Zaumseil for the access to the infrastructure at the Chair of Applied Physical Chemistry.

## REFERENCES

- Rowell, J. L. C.; Yaghi, O. M. Metal-organic frameworks: A new class of porous materials. *Microporous Mesoporous Mater.* **2004**, *73*, 3–14.
- Bauer, S.; Stock, N. Hochdurchsatz-Methoden in der Festkörperchemie. Schneller zum Ziel. *Chem. Unserer Zeit* **2007**, *41*, 390–398.
- Zhang, M.; Li, H.; Perry, Z.; Zhou, H.-C. Gas Storage in Metal-Organic Frameworks. *Encyclopedia of Inorganic and Bioinorganic (EDS.: Scott, Robert A.)*; Wiley, 2011.
- Shekha, O.; Chernikova, V.; Belmabkhout, Y.; Eddaoudi, M. Metal-Organic Framework Membranes: From Fabrication to Gas Separation. *Crystals* **2018**, *8*, 412.
- Wang, C.; An, B.; Lin, W. Metal-Organic Frameworks in Solid-Gas Phase Catalysis. *ACS Catal.* **2018**, *9*, 130–146.
- Xiao, J.-D.; Jiang, H.-L. Metal-Organic Frameworks for Photocatalysis and Photothermal Catalysis. *Acc. Chem. Res.* **2019**, *52*, 356–366.
- Kim, H.; Yang, S.; Rao, S. R.; Narayanan, S.; Kapustin, E. A.; Furukawa, H.; Umans, A. S.; Yaghi, O. M.; Wang, E. N. Water harvesting from air with metal-organic frameworks powered by natural sunlight. *Science* **2017**, *356*, 430–434.
- Henninger, S. K.; Ernst, S.-J.; Gordeeva, L.; Bendix, P.; Fröhlich, D.; Grekova, A. D.; Bonaccorso, L.; Aristov, Y.; Jaenchen, J. New materials for adsorption heat transformation and storage. *Renewable Energy* **2017**, *110*, 59–68.
- Jeremias, F.; Fröhlich, D.; Janiak, C.; Henninger, S. K. Water and methanol adsorption on MOFs for cycling heat transformation processes. *New J. Chem.* **2014**, *38*, 1846–1852.
- Chen, W.; Wu, C. Synthesis, functionalization, and applications of metal-organic frameworks in biomedicine. *Dalton Trans.* **2018**, *47*, 2114–2133.
- Wu, M.-X.; Yang, Y.-W. Metal-Organic Framework (MOF)-Based Drug/Cargo Delivery and Cancer Therapy. *Adv. Mater.* **2017**, *29*, 1606134.
- Li, Y.; Xiao, A.-S.; Zou, B.; Zhang, H.-X.; Yan, K.-L.; Lin, Y. Advances of metal-organic frameworks for gas sensing. *Polyhedron* **2018**, *154*, 83–97.
- Vikrant, K.; Kumar, V.; Ok, Y. S.; Kim, K.-H.; Deep, A. Metal-organic framework (MOF)-based advanced sensing platforms for the detection of hydrogen sulfide. *Trends Anal. Chem.* **2018**, *105*, 263–281.
- Lu, K.; Aung, T.; Guo, N.; Weichselbaum, R.; Lin, W. Nanoscale Metal-Organic Frameworks for Therapeutic, Imaging, and Sensing Applications. *Adv. Mater.* **2018**, *30*, e1707634.
- Liu, D.; Lu, K.; Poon, C.; Lin, W. Metal-organic frameworks as sensory materials and imaging agents. *Inorg. Chem.* **2014**, *53*, 1916–1924.
- Liu, D.; Zou, D.; Zhu, H.; Zhang, J. Mesoporous Metal-Organic Frameworks: Synthetic Strategies and Emerging Applications. *Small* **2018**, *14*, e1801454.
- Song, L.; Zhang, J.; Sun, L.; Xu, F.; Li, F.; Zhang, H.; Si, X.; Jiao, C.; Li, Z.; Liu, S.; Liu, Y.; Zhou, H.; Sun, D.; Du, Y.; Cao, Z.; Gabelica, Z. Mesoporous metal-organic frameworks: Design and applications. *Energy Environ. Sci.* **2012**, *5*, 7508.
- Bosch, M.; Zhang, M.; Zhou, H.-C. Increasing the Stability of Metal-Organic Frameworks. *Adv. Chem.* **2014**, *2014*, 1–8.
- Cavka, J. H.; Jakobsen, S.; Olsbye, U.; Guillou, N.; Lamberti, C.; Bordiga, S.; Lillerud, K. P. A new zirconium inorganic building brick forming metal organic frameworks with exceptional stability. *J. Am. Chem. Soc.* **2008**, *130*, 13850–13851.
- Kim, M.; Cohen, S. M. Discovery, development, and functionalization of Zr(IV)-based metal-organic frameworks. *CrystEngComm* **2012**, *14*, 4096–4104.
- Peh, S. B.; Cheng, Y.; Zhang, J.; Wang, Y.; Chan, G. H.; Wang, J.; Zhao, D. Cluster nuclearity control and modulated hydrothermal synthesis of functionalized Zr12 metal-organic frameworks. *Dalton Trans.* **2019**, *48*, 7069–7073.
- Ji, P.; Manna, K.; Lin, Z.; Feng, X.; Urban, A.; Song, Y.; Lin, W. Single-Site Cobalt Catalysts at New Zr12(μ<sub>3</sub>-O)8(μ<sub>3</sub>-OH)8(μ<sub>2</sub>-OH)6 Metal-Organic Framework Nodes for Highly Active Hydrogenation of Nitroarenes, Nitriles, and Isocyanides. *J. Am. Chem. Soc.* **2017**, *139*, 7004–7011.
- Waitschat, S.; Reinsch, H.; Arpacioğlu, M.; Stock, N. Direct water-based synthesis and characterization of new Zr/Hf-MOFs with dodecanuclear clusters as IBUs. *CrystEngComm* **2018**, *20*, 5108–5111.
- Cliffe, M. J.; Castillo-Martínez, E.; Wu, Y.; Lee, J.; Forse, A. C.; Firth, F. C. N.; Moghadam, P. Z.; Fairen-Jimenez, D.; Gaultois, M. W.; Hill, J. A.; Magdysyuk, O. V.; Slater, B.; Goodwin, A. L.; Grey, C. P. Metal-Organic Nanosheets Formed via Defect-Mediated Transformation of a Hafnium Metal-Organic Framework. *J. Am. Chem. Soc.* **2017**, *139*, 5397–5404.
- Waitschat, S.; Reinsch, H.; Stock, N. Water-based synthesis and characterisation of a new Zr-MOF with a unique inorganic building unit. *Chem. Commun.* **2016**, *52*, 12698–12701.
- Leubner, S.; Zhao, H.; van Velthoven, N.; Henrion, M.; Reinsch, H.; Vos, D. E. de; Kolb, U.; Stock, N. Expanding the Variety of Zirconium-based Inorganic Building Units for Metal-Organic Frameworks. *Angew. Chem. Int. Ed.* **2019**, *58*, 10995–11000.
- Prat, D.; Hayler, J.; Wells, A. A survey of solvent selection guides. *Green Chem* **2014**, *16*, 4546–4551.
- Vidra, A.; Németh, Á. Bio-produced Acetic Acid: A Review. *Period. Polytech. Chem. Eng.* **2018**, *62*, 245–256.
- Zhao, M.; Huang, Y.; Peng, Y.; Huang, Z.; Ma, Q.; Zhang, H. Two-dimensional metal-organic framework nanosheets: Synthesis and applications. *Chem. Soc. Rev.* **2018**, *47*, 6267–6295.
- Hu, G.; Kang, J.; Ng, L. W. T.; Zhu, X.; Howe, R. C. T.; Jones, C. G.; Hersam, M. C.; Hasan, T. Functional inks and printing of two-dimensional materials. *Chem. Soc. Rev.* **2018**, *47*, 3265–3300.
- Bonaccorso, F.; Bartolotta, A.; Coleman, J. N.; Backes, C. 2D-Crystal-Based Functional Inks. *Adv. Mater.* **2016**, *28*, 6136–6166.
- Backes, C.; Campi, D.; Szydłowska, B. M.; Synnatschke, K.; Ojala, E.; Rashvand, F.; Harvey, A.; Griffin, A.; Sofer, Z.; Marzari, N.; Coleman, J. N.; O'Regan, D. D. Equipartition of Energy Defines the Size-Thickness Relationship in Liquid-Exfoliated Nanosheets. *ACS Nano* **2019**, *13*, 7050–7061.
- Nicolosi, V.; Chhowalla, M.; Kanatzidis, M. G.; Strano, M. S.; Coleman, J. N. Liquid Exfoliation of Layered Materials. *Science* **2013**, *340*, 1226419.
- Lange, R. Z.; Synnatschke, K.; Qi, H.; Huber, N.; Hofer, G.; Liang, B.; Huck, C.; Pucci, A.; Kaiser, U.; Backes, C.; Schlüter, A. D. Enriching and Quantifying Porous Single Layer 2D Polymers by Exfoliation of Chemically Modified van der Waals Crystals. *Angew. Chem. Int. Ed.* **2020**, *59*, 5683–5695.

- (35) Kang, J.; Sangwan, V. K.; Wood, J. D.; Hersam, M. C. Solution-Based Processing of Monodisperse Two-Dimensional Nanomaterials. *Acc. Chem. Res.* **2017**, *50*, 943–951.
- (36) Backes, C.; Szydłowska, B. M.; Harvey, A.; Yuan, S.; Vega-Mayoral, V.; Davies, B. R.; Zhao, P.-L.; Hanlon, D.; Santos, E. J. G.; Katsnelson, M. I.; Blau, W. J.; Gadermaier, C.; Coleman, J. N. Production of Highly Monolayer Enriched Dispersions of Liquid-Exfoliated Nanosheets by Liquid Cascade Centrifugation. *ACS Nano* **2016**, *10*, 1589–1601.
- (37) Stock, N. High-throughput investigations employing solvothermal syntheses. *Microporous Mesoporous Mater.* **2010**, *129*, 287–295.
- (38) Xu, H.; Lebrette, H.; Yang, T.; Srinivas, V.; Hovmöller, S.; Högbom, M.; Zou, X. A Rare Lysozyme Crystal Form Solved Using Highly Redundant Multiple Electron Diffraction Datasets from Micron-Sized Crystals. *Structure* **2018**, *26*, 667–675.e3.
- (39) Wang, B.; Zou, X.; Smeets, S. Automated serial rotation electron diffraction combined with cluster analysis: An efficient multi-crystal workflow for structure determination. *IUCrJ* **2019**, *6*, 854–867.
- (40) Feng, D.; Liu, T.-F.; Su, J.; Bosch, M.; Wei, Z.; Wan, W.; Yuan, D.; Chen, Y.-P.; Wang, X.; Wang, K.; Lian, X.; Gu, Z.-Y.; Park, J.; Zou, X.; Zhou, H.-C. Stable metal-organic frameworks containing single-molecule traps for enzyme encapsulation. *Nat. Commun.* **2015**, *6*, 5979.
- (41) Feng, D.; Wang, K.; Su, J.; Liu, T.-F.; Park, J.; Wei, Z.; Bosch, M.; Yakovenko, A.; Zou, X.; Zhou, H.-C. A highly stable zeotype mesoporous zirconium metal-organic framework with ultralarge pores. *Angew. Chem. Int. Ed.* **2015**, *54*, 149–154.
- (42) Wan, W.; Sun, J.; Su, J.; Hovmöller, S.; Zou, X. Three-dimensional rotation electron diffraction: Software RED for automated data collection and data processing. *J. Appl. Crystallogr.* **2013**, *46*, 1863–1873.
- (43) Zhang, X.; Zhang, X.; Johnson, J. A.; Chen, Y.-S.; Zhang, J. Highly Porous Zirconium Metal-Organic Frameworks with  $\beta$ -UH3-like Topology Based on Elongated Tetrahedral Linkers. *J. Am. Chem. Soc.* **2016**, *138*, 8380–8383.
- (44) Shearer, G. C.; Vitillo, J. G.; Bordiga, S.; Svelle, S.; Olsbye, U.; Lillerud, K. P. Functionalizing the Defects: Postsynthetic Ligand Exchange in the Metal Organic Framework UiO-66. *Chem. Mater.* **2016**, *28*, 7190–7193.
- (45) Mondloch, J. E.; Bury, W.; Fairen-Jimenez, D.; Kwon, S.; DeMarco, E. J.; Weston, M. H.; Sarjeant, A. A.; Nguyen, S. T.; Stair, P. C.; Snurr, R. Q.; Farha, O. K.; Hupp, J. T. Vapor-phase metalation by atomic layer deposition in a metal-organic framework. *J. Am. Chem. Soc.* **2013**, *135*, 10294–10297.
- (46) Fu, G.; Bueken, B.; Vos, D. de. Zr - Metal - Organic Framework Catalysts for Oxidative Desulfurization and Their Improvement by Postsynthetic Ligand Exchange. *Small Methods* **2018**, *2*, 1800203.
- (47) van de Voorde, B.; Stassen, I.; Bueken, B.; Vermoortele, F.; Vos, D. de; Ameloot, R.; Tan, J.-C.; Bennett, T. D. Improving the mechanical stability of zirconium-based metal-organic frameworks by incorporation of acidic modulators. *J. Mater. Chem. A* **2015**, *3*, 1737–1742.
- (48) Marshall, R. J.; Forgan, R. S. Postsynthetic Modification of Zirconium Metal-Organic Frameworks. *Eur. J. Inorg. Chem.* **2016**, *2016*, 4310–4331.
- (49) Thommes, M.; Kaneko, K.; Neimark, A. V.; Olivier, J. P.; Rodriguez-Reinoso, F.; Rouquerol, J.; Sing, K. S.W. Physisorption of gases, with special reference to the evaluation of surface area and pore size distribution (IUPAC Technical Report). *Pure Appl. Chem.* **2015**, *87*, 1051–1069.
- (50) Ogilvie, S. P.; Large, M. J.; O'Mara, M. A.; Lynch, P. J.; Lee, C. L.; King, A. A. K.; Backes, C.; Dalton, A. B. Size selection of liquid-exfoliated 2D nanosheets. *2D Mater.* **2019**, *6*, 31002.
- (51) Backes, C.; Smith, R. J.; McEvoy, N.; Berner, N. C.; McCloskey, D.; Nerl, H. C.; O'Neill, A.; King, P. J.; Higgins, T.; Hanlon, D.; Scheuschner, N.; Maultzsch, J.; Houben, L.; Duesberg, G. S.; Donegan, J. F.; Nicolosi, V.; Coleman, J. N. Edge and confinement effects allow in situ measurement of size and thickness of liquid-exfoliated nanosheets. *Nat. Commun.* **2014**, *5*, 4576.
- (52) Niu, Y.; Gonzalez-Abad, S.; Frisenda, R.; Maruhn, P.; Drüppel, M.; Gant, P.; Schmidt, R.; Taghavi, N. S.; Barcons, D.; Molina-Mendoza, A. J.; Vasconcellos, S. M. de; Bratschitsch, R.; Perez De Lara, D.; Rohlfing, M.; Castellanos-Gomez, A. Thickness-Dependent Differential Reflectance Spectra of Monolayer and Few-Layer MoS<sub>2</sub>, MoSe<sub>2</sub>, WS<sub>2</sub> and WSe<sub>2</sub>. *Nanomaterials* **2018**, *8*, 725.
- (53) Harvey, A.; Backes, C.; Boland, J. B.; He, X.; Griffin, A.; Szydłowska, B.; Gabbett, C.; Donegan, J. F.; Coleman, J. N. Non-resonant light scattering in dispersions of 2D nanosheets. *Nat. Commun.* **2018**, *9*, 4553.

1  
2  
3  
4  
5  
6  
7  
8  
9  
10  
11  
12  
13  
14  
15  
16  
17  
18  
19  
20  
21  
22  
23  
24  
25  
26  
27  
28  
29  
30  
31  
32  
33  
34  
35  
36  
37  
38  
39  
40  
41  
42  
43  
44  
45  
46  
47  
48  
49  
50  
51  
52  
53  
54  
55  
56  
57  
58  
59  
60

